remote sensing

MDPI

Article

Inversion of Boreal Forest Height Using the CRITIC Weighted Least Squares Three-Stage Temporal Decorrelation Iterative Algorithm

Ao Sui and Wenyi Fan *

Key Laboratory of Sustainable Forest Ecosystem Management-Ministry of Education, School of Forestry, Northeast Forestry University, Harbin 150040, China; suiao_2019@nefu.edu.cn
* Correspondence: fanwy@nefu.edu.cn; Tel.: +86-139-4605-5384

Abstract: The inversion of forest height using the RVoG (Random Volume over Ground) model is susceptible to overestimation or underestimation due to three error sources, propagating inaccuracies to the estimated forest height. Furthermore, variations in the height and density of the scenario could impact how well the RVoG three-stage inversion performs. This work utilizes the L-band single-baseline full polarization interferometric dataset as its basis. It optimally applies the CRITIC (Criteria Importance Through Intercriteria Correlation) method to the first stage of a three-stage process. This approach aims to overcome the issues mentioned above and enhance the accuracy of forest parameter estimation. A CRITIC weighted least squares temporal decoherence iterative algorithm is also proposed for the characteristics of the spaceborne data, in combination with the temporal decoherence algorithm of previous research. The proposed approach is tested and applied to both simulated and actual data. The optimization approach is first assessed using four simulated datasets that simulate coniferous forests with different densities and heights. The preliminary findings suggest that optimizing the complex coherence fitting process through the weighted least squares method enhances the accuracy of ground phase estimation and, consequently, improves the accuracy of the three-stage approach for inverting forest height. The ground phase estimation results for low forest height consistently remained within 0.02 rad, with a root mean square error (RMSE) below 0.05 rad, and no saturation occurred with increasing forest density. The enhanced algorithm outperforms the traditional technique in terms of accuracy in ground phase estimation. Subsequently, the optimized approach is applied to ALOS-2 spaceborne data, proving more successful than the conventional algorithm in reducing the RMSE of forest height. The findings illustrate the method's superior inversion performance, obtaining an accuracy exceeding 80% in both the test and validation sets. The validation set's RMSE is approximately 2.5 m, and the mean absolute error (MAE) is within 2 m. Moreover, it is observed that to counteract the uncertainty in temporal decoherence induced by climate change, a larger temporal baseline necessitates a larger random motion compensation term and phase offset term.

Keywords: PolInSAR; RVoG; forest height; three-stage model; ground phase; temporal decorrelation

Citation: Sui, A.; Fan, W. Inversion of Boreal Forest Height Using the CRITIC Weighted Least Squares Three-Stage Temporal Decorrelation Iterative Algorithm. *Remote Sens.* **2024**, *16*, 1137. https://doi.org/10.3390/rs16071137

Academic Editors: Heiko Balzter and Markus Immitzer

Received: 14 February 2024
Revised: 17 March 2024
Accepted: 21 March 2024
Published: 25 March 2024

1. Introduction

Forests play a pivotal role as a critical component of terrestrial ecosystems. Achieving accurate estimates of the carbon content in forests is crucial for initiatives to enhance forest quality. A fundamental metric in this endeavor is the precise inversion of forest height, indicating vegetation structure [1]. Widespread remote sensing applications include monitoring large-scale regional changes in forests, ice caps, mountains, oceans, and other environments. According to a literature review, optical remote sensing is better suited to capturing the horizontal structure of forest stands. Information on vegetation index, texture, and spectral responses is leveraged to facilitate modeling optical remote sensing data [2,3].

Jung, H et al. used different vegetation indexes to assess the vegetation activity in the Korean Peninsula, and the results of the study showed that different vegetation indexes can be utilized to monitor vegetation drought changes in different months [4]. While Lidar can capture the vertical structure of forest stands, its widespread application is hindered by high costs and limited point cloud utilization, rendering it impractical for extensive regions [5]. In evaluating the vertical structure of forest areas, synthetic aperture radar (SAR) proves more suitable than optical remote sensing and LiDAR. Despite weather conditions, SAR's ability to penetrate forests consistently is valuable for regions with frequent rainfall and snowfall [6,7]. Furthermore, SAR's capability to work with different frequency bands, multiple polarizations, and multiple baselines supports the inversion of forest vertical structure parameters. Currently, polarimetric SAR (PolSAR), interferometric SAR (InSAR), polarization interferometric SAR (PolInSAR), and tomographic SAR (TomoSAR) are among the most advanced earth observation methods employed globally.

One commonly employed tool for forest height inversion with SAR is the RVoG model within the single-baseline PolInSAR approach. By integrating the capabilities of PolSAR with InSAR, PolInSAR facilitates the extraction of vertical position information from various scatterers by creating interferograms across different polarization channels [8]. The essence of the RVoG model for forest height inversion lies in utilizing different polarizations to differentiate the central phase of the forest canopy from the ground phase. Subsequently, the interferometric phase is employed to estimate vegetation height [9]. This process has three predominant error sources in PolInSAR: non-volume decoherence, the ground phase error, and the residual ground component in the polarization channel [10]. For L-band data, the residual ground-to-volume scattering ratio (GVR) in the volume polarization channel is considered to be 0 [11,12]. Non-volume decoherence encompasses geometric, temporal, and signal-to-noise ratio decoherence of interferometric echoes [13], with temporal decoherence being the primary contributor, as geometric decoherence and signal-to-noise decoherence can be corrected during SAR pre-processing [14]. The primary error sources in forest height inversion from spaceborne data include ground phase estimate errors and temporal decoherence, particularly for spaceborne SAR data with long-time baselines. Temporal decoherence, observed in both L-band and P-band, increases with increasing temporal baseline, leading to reduced inversion precision, overestimated forest height, and diminished observational coherence [15]. A study by [15] revealed a mean forest height overestimation of 6 m with a 30-day temporal baseline, with potential additional local biases. Due to the L-band's shorter wavelength than the P-band, its coherence is more affected by temporal decoherence than that of the P-band [15,16]. In scenarios involving airborne SAR or simulated data, temporal decoherence can be effectively considered zero, given the shorter time baseline. For spaceborne SAR data, improved temporal decoherence methods have been proposed. Yongxin Zhang et al. showed that datasets with a long spatial baseline and long wavelength have a positive effect on the inversion of forest height [17]. Mao et al. [18]. suggested a multiple iteration temporal decoherence approach for the spaceborne ALOS-2 data due to its short baseline and tiny vertical wavenumber. Even if the model's error for tree height is only 15%, the model only uses one vertical wave number and more iteration parameters throughout the entire map, which is devoid of topographical detail information. Rula Sa et al. [19] improved Mao's model by introducing an extinction coefficient that varies with height as well as constructing a new complex coherence using polarization decomposition to reduce excessive ground contributions in sparse vegetation. However, the algorithm lacks a validation set to test the accuracy of the empirical parameters. The resulting tree height map is severely fragmented when this empirical parameter is applied to the entire area mapping process.

Controlling the impact of ground phase errors on the inversion process is crucial, as these errors propagate to other forest parameters. [20] presented a method for error assessment at each stage of their three-stage analysis, focusing on ground phase errors induced by geometric parameters of the coherence region in the RVoG model. Geometric factors, such as the phase difference between the long axis and the unit circle or the narrow-to-width ratio of the coherence ellipse, are influenced by surface features. Consequently, various factors, including the vertical structure of the forest (forest height and density), affect the inversion of the ground phase. Dense forests reduce dihedral reflections in the coherence phase, which results in lower interferometric phase separation, then the shape of the coherence region is closer to a circle, resulting in a low accuracy of ground phase estimation in the three-stage process [21]. In the case of electromagnetic waves, signals attenuate as they enter the forest canopy, and the RVoG model uses an extinction coefficient to represent signal attenuation. An inverse correlation exists between the penetration depth and the extinction coefficient, where signal attenuation increases with forest density, leading to a decrease in penetration depth [22]. In InSAR, the penetration depth is affected by the canopy and ground phase difference, consequently influencing the offsets in the ground phase center with the degree of electromagnetic wave attenuation. We hypothesize that improving the accuracy of ground phase estimates in the three-stage model will enhance the performance of the forest height mode.

One of our contributions involves introducing an optimization algorithm to enhance ground phase estimation accuracy. Utilizing the PolSARpro SIM toolbox within the ESA PolSARpro v6.0.2 software for simulation experiments [23], we point out the significance of ground phases in forest parameter inversion and the impact of associated errors. To optimize the conventional three-stage inversion process, our approach incorporates the CRITIC weighted least squares algorithm and the coherence optimization algorithm. Subsequently, it applies various sets of simulated datasets representing forest height–density scenarios to estimate forest height. This study significantly contributes to enhancing the iterative algorithm for temporal decoherence. It delves into the impact of temporal decoherence on the forest height retrieval process in PolInSAR inversion. This study uses two sets of ALOS2 PALSAR2 spaceborne L-band data with different temporal baselines to validate the algorithm's feasibility on real datasets.

2. Datasets and Pre-Processing

2.1. Simulated Dataset

The efficacy of the improved algorithm was investigated in this study under scenarios of total forest density, along with an assessment of the influence of changing forest densities and heights on the PolInSAR forest height inversion process. Simulated datasets were generated using the PolSARproSim module within the PolSARpro v6.0.2 software to mitigate the impact of temporal decoherence and other variables such as terrain and climate. This toolbox creates ideal polarization interferometric images without issues like temporal, signal-to-noise ratio decoherence, and co-registration errors [24,25].

After reviewing the information, it was identified that the main tree species in the real dataset was coniferous forest, with a percentage of forest stock volume of 78.7%, so coniferous forest was also selected for the simulation dataset. In addition, the average forest height in the study area is less than 25 m. The simulation datasets of 10 m, 14 m, 18 m, and 22 m were chosen to represent the whole study area. It is also possible to explore the effect of different heights on the ground phase. Nine kinds of forest densities were established for each forest height, spanning from 100 stems/ha to 900 stems/ha. The scenes of the simulated dataset are presented in Figure A1, and all simulated datasets are based on airborne L-band fully polarization interferometric SAR with identical parameters, as detailed in Table 1.

Table 1. Specific parameters of the simulated dataset.

Platform Configuration	Parameter	Forest/Ground Surface Configuration	Parameter
Platform Altitude	3000 m	Tree Species	Pine
Horizontal/Vertical Baseline	10 m, 1 m	Surface Properties/Ground Moisture Content	0, 0
Incidence Angle	45°	Azimuth/Range Ground Slope	0, 0
Centre Frequency	1.3 GHZ	Tree Height	10 m\14 m\18 m\22 m

2.2. The ALOS-2 PALSAR-2 Dataset

2.2.1. Overview of the Study Area

The research site is the Saihanba Forest Farm in Chengde City, Hebei Province, China. The Saihanba Forest Farm actively engages in afforestation and forest management carbon sink initiatives, which are approved under the Chinese Certified Emission Reduction (CCER) scheme [26]. In addition to actively responding to the United Nations Forest Instrument, the Saihanba Forest Farm keeps looking into new approaches to high-quality forestry development. Thus, mapping and monitoring the Saihanba Forest Farm requires interferometric synthetic aperture radar (SAR). In Figure 1, the black image represents the Saihanba Forest Farm range's 95% coverage, while the red line delineates its boundary. The average slope of the region is 9.86°. Figure A2 presents the detailed elevation and slope information for the study area.

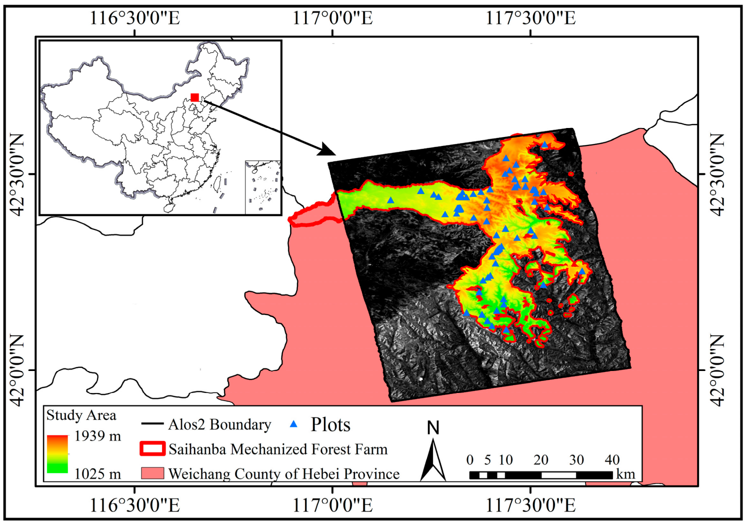

Figure 1. China's Saihanba Mechanical Forest and Research Area is in Weichang County, Hebei Province. The red line region delineates the entire extent of the Sehamba Mechanical Forest. The pink area on the map corresponds to Weichang County. The black quadrilateral area denotes the SAR image coverage, exemplified using the 11 July 2020 image, while the blue triangles on the images signify the sample plots utilized in the field survey.

2.2.2. Forest Inventory Data

Custom programming generated the ALOS-2 dataset between July and September 2020. Due to the unpredictability and uncertainty of the customized data throughout this period, a real-time field survey of the research area was not feasible in 2020. Consequently, in August 2021, during the boreal temperate forest's growing season, the team conducted a field survey of the Saihanba Mechanical Forest (Figure A3). 72 sample plots of 0.06 ha were established during the field investigation, all located in coniferous forests. We also ensured the sample plots (blue triangles) were evenly distributed throughout the study area to enhance representativeness. Figure 2 displays the sample plots' Q-Q plots and normal distribution histograms, indicating an average tree height of 15.61 m. The sample plots exhibited an excellent normal distribution without any exceptional values.

2.2.3. SAR Data and Pre-Processing

The JAXA (Japan Aerospace and Exploration Agency) Land Observing Satellite mission ALOS-2 [6] aims to provide data support for environmental monitoring, mapping, disaster monitoring, and other applications. As a successor to ALOS, ALOS-2 incorporates the PALSAR-2 sensor for day and night observation of the study area. The utilization of fully polarized L-band (1.27 GHz) Synthetic Aperture Radar (SAR) data not only enhances capability but also reduces the satellite revisit period from 46 days to 14 days [27]. However, its interferometric ability is still constrained by the temporal baseline, leading to lower coherence affecting forest parameter estimation.

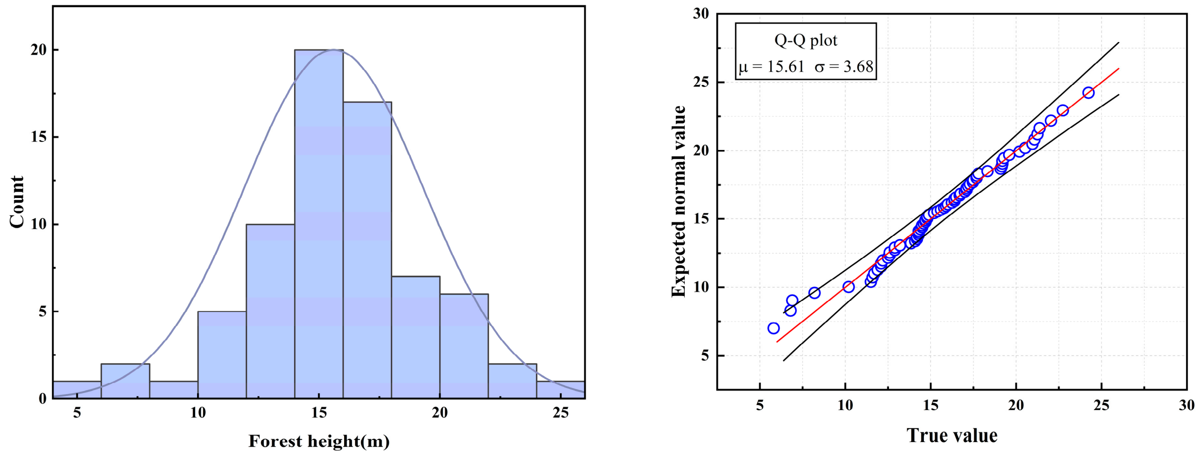

(**a**) (**b**)

Figure 2. (**a**) Frequency histogram of the sample plots. (**b**) Q-Q plot of the sample plots, where the blue circle represents the sample and the red line represents the 1:1 line.

This study selected three images from the ALOS-2 collection. The specific SAR data, including acquisition time, incidence angle, spatial resolution, and center slant distance, are presented in Table 2. The dataset consists of L-band single-look complex (SLC) Level 1.1 SAR products in StripMap mode with full polarization. The spatial resolution of the image in the slant–azimuth SAR coordinate system is 2.86 m × 2.64 m (slant range × azimuth).

Table 2. Specific parameters of the ALOS-2 PALSAR-2 datasets.

Acquisition SAR Dates	Level	Polarization	Incidence Angle	Spatial Resolution (Rg × Az)	Center Range (SLC)
11 July 2020	L1.1 CEOS	Full (Quad.)	27.8054°	2.86 m × 2.64 m	710,741.6730 m
25 July 2020	L1.1 CEOS	Full (Quad.)	27.8029°	2.86 m × 2.64 m	710,741.6730 m
19 September 2020	L1.1 CEOS	Full (Quad.)	27.7975°	2.86 m × 2.64 m	710,741.6730 m

This study employed three images, detailed in Table 3, consisting of two sets of interferometric pairs with temporal baselines of 14 and 90 days, respectively. PolSARpro v6.0.2 software and GAMMA software (http://www.gamma-rs.ch) were used for SAR pre-processing and geocoding, respectively. Major pre-processing steps included radiometric calibration, multilooking, speckle filtering, atmospheric ionospheric filtering, and complex coherence generation. Multilooking in the SAR image involved nine azimuth and four range directions, with 7 × 7 LEE refined speckle filtering applied to eliminate coherence speckle noise [28]. The dimensions of the multi-looking image were 2098 pixels × 2900 pixels, and the ground range resolution is range × azimuth = 25.31 m × 23.76 m. Figure 3 showed the pre-processed interferometric image and the DEM image of the study area.

Table 3. Details for two pairs of interferometric pairs.

Master Image	Slave Image	Mean kz (rad/m)	Temporal Baseline (Day)
11 July 2020	25 July 2020	0.0144	14
11 July 2020	19 September 2020	0.0201	70

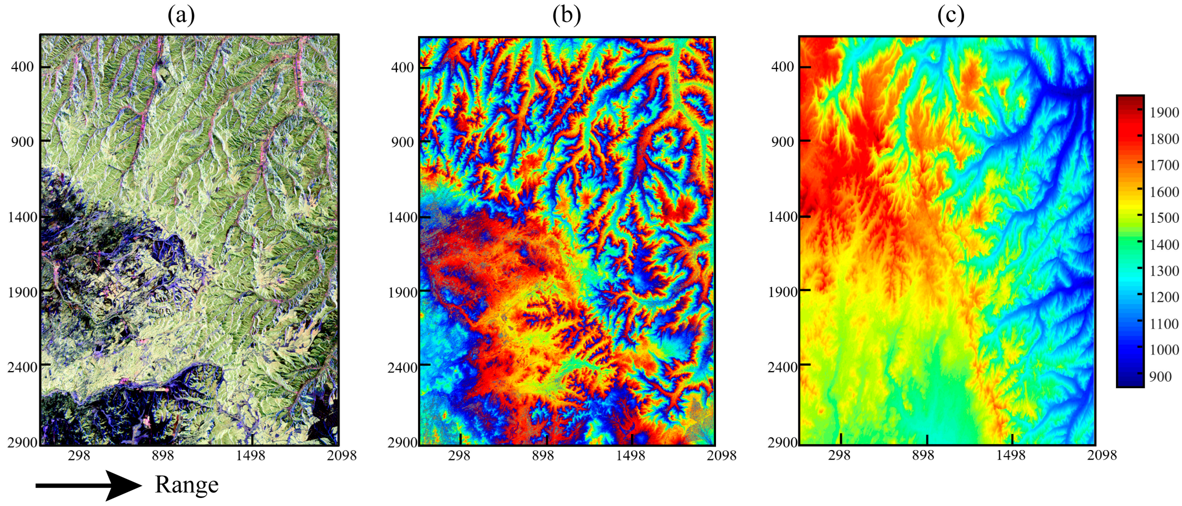

Figure 3. The ALOS-2 PALSAR-2 fully polarization image of 11 July 2020 is an example. (**a**) displays a Pauli-based RGB map where |HH − VV| is represented in red, |HV| in green, and |HH + VV| in blue. (**b**) The interferogram removal of atmospheric-ionospheric effects. (**c**) A DEM image in SAR coordinates with 30 m × 30 m resolution SRTM-DEM.

2.2.4. Weather Condition

In this study, the Weichang County weather station, which records weather data every three hours, provided the weather information. Figure 4 illustrates the weather conditions for the day of the three image acquisitions and the three preceding days. There was no precipitation on 11 July, 25 July, or the three days before. While 19 September had no rain, 16 September experienced some rainfall. Wind conditions influenced the movement of leaves and branches throughout the image acquisition periods.

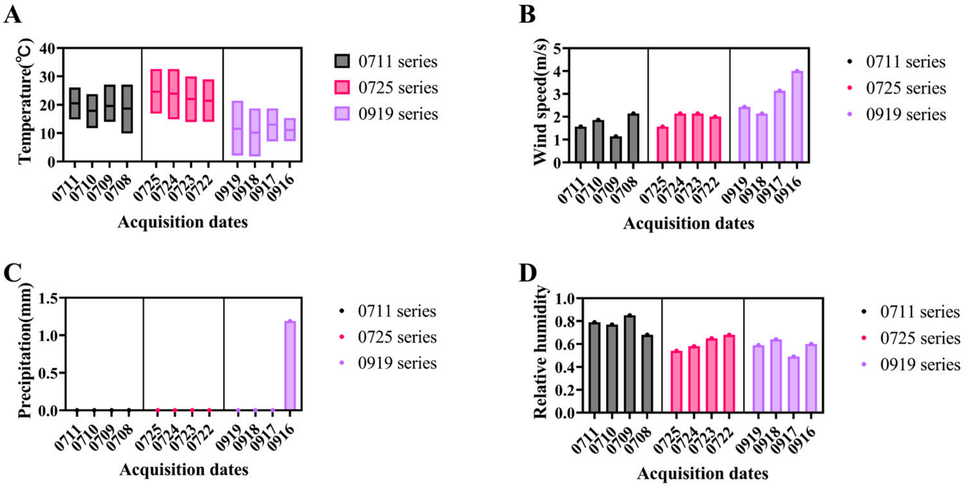

Figure 4. The day of the three SAR images and the preceding three days depict the weather conditions. (**A**) represents temperature variation, with the middle line indicating the average temperature and the lower and upper lines denoting the minimum and maximum temperatures, respectively. (**B**) illustrates the average wind speed, and (**C**) depicts precipitation. (**D**) shows the relative humidity.

Additionally, there was no snowfall on the days corresponding to the three images and the preceding days. On 19 September, the lowest temperature recorded was 2.1 °C, while the highest temperature differential recorded was 20 °C. No sub-freezing temperatures were recorded during the monitoring times, indicating non-freezing scenarios [29].

3. The CRITIC-ITDRvoG Algorithm

3.1. The RVoG Method

Cloude et al. resolved the RVoG model into a straight-line structure (Equation (1)) and divided the forest structure into a uniformly dense volume layer and a ground layer. They used the property that complex coherences with different polarizations exhibit a straight-line distribution in the complex unit circle. However, it is noteworthy that they did not consider noise decoherence, temporal decoherence, or other decoherence assumptions.

$$\gamma(w) = e^{j\phi_{ground}}[\gamma_v + L_w(1-\gamma_v)],\ L_w = \frac{m(w)}{1+m(w)}, \tag{1}$$

$$\gamma_v = \frac{2\sigma}{2\sigma+jk_z\cos\theta}\cdot\frac{exp(2\sigma h_v/\cos\theta+jk_zh_v)-1}{exp(2\sigma h_v/\cos\theta)-1},\quad k_z = \frac{4\pi B_\perp}{\lambda Rsin\theta}, \tag{2}$$

where γ_v denotes the pure volume complex coherence of the forest canopy, $m(w)$ represents the ground-to-volume scattering ratio for a specific polarization mode, L_w signifies the ground scattering ratio, and ϕ_{ground} corresponds to the ground phase. Additionally, σ denotes the vegetation extinction coefficient, indicating the energy attenuation of electromagnetic waves caused by the canopy structure, θ embodies the angle of incidence of the master image radar, and k_z denotes the vertical wavenumber.

The three-stage approach divides the quantitative inversion process of vegetation parameters into three stages (Figure 5): (a) employing the ordinary least squares method to fit straight lines in the complex unit circle for each complex coherence, with a refined explanation provided in the subsequent section; (b) determining the actual ground phase through the intersection of the fitted straight line with the complex unit circle; and (c) inverting forest heights and extinction coefficients by constructing a height–extinction coefficient two-dimensional lookup table $LUT(h_v, \sigma)$ following Equation (2). The pure volume layer γ_v is a polarization-independent function that only varies with the vegetation height h_v and extinction coefficient σ [11]. The available research suggests that the extinction coefficient does not significantly impact the inversion error. Thus, for this study, the assumption is made that the extinction coefficient is 0.5 dB/m. Under this assumption, the forest height inversion process is represented by Equation (3), leading to improved inversion efficiency. Identifying the minimum value between the assumed pure volume coherence γ_{V-assu} and the pure volume coherence established through the lookup table determines the corresponding forest height.

$$height = \underset{(height)}{argmin}\left\{\left|\gamma_{V-assu}e^{-i\phi_{ground}} - LUT(h_v, \sigma = 0.4)\right|\right\}, \tag{3}$$

Vertical baseline, slant range, wavelength, and radar incidence angle influence the vertical wavenumber k_z. Many studies have indicated that the theoretical model of forest scattering is sensitive to terrain slope, mainly due to terrain fluctuations in the Saihanba area. A higher terrain slope corresponds to increased inversion errors in forest height. Our study incorporates the local incidence angle ϕ_0 to correct the vertical wavenumber in the forest scattering mode to correct terrain effects. Figure 6 illustrates the two sets of ALOS-2 vertical wavenumbers after correction.

$$\theta_0 = \theta - \alpha, \tag{4}$$

$$k_{z0} = \frac{4\pi B_\perp}{\lambda Rsin\theta_0}, \tag{5}$$

3.2. The CRITIC-WLS Algorithm

This study utilizes the CRITIC method to ascertain the weight assigned to each coherence in the first stage of the traditional three-stage algorithm. In this study, n complex coherences fit straight lines, where the real and imaginary parts of the complex coherences act as the evaluation samples (m = 2), and the complex coherence acts as assessment criteria.

$$X = \begin{pmatrix} x_{11} & \cdots & x_{1n} \\ \vdots & \ddots & \vdots \\ x_{m1} & \cdots & x_{mn} \end{pmatrix}, \tag{6}$$

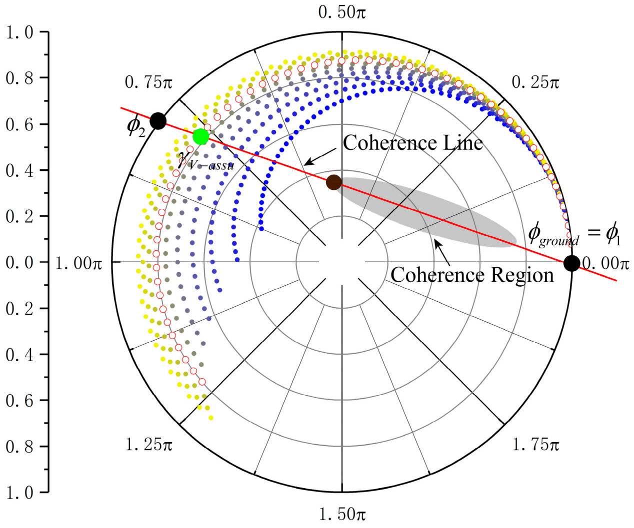

Figure 5. The figure depicts the three-stage algorithm. The colored points represent 2D lookup tables, with the red circle representing the lookup table for a fixed extinction coefficient. The green points indicate the assumed pure volume complex coherence points. The black points denote the intersection points of the coherence straight line and the complex coherence circle, i.e., the points to determine the ground phase.

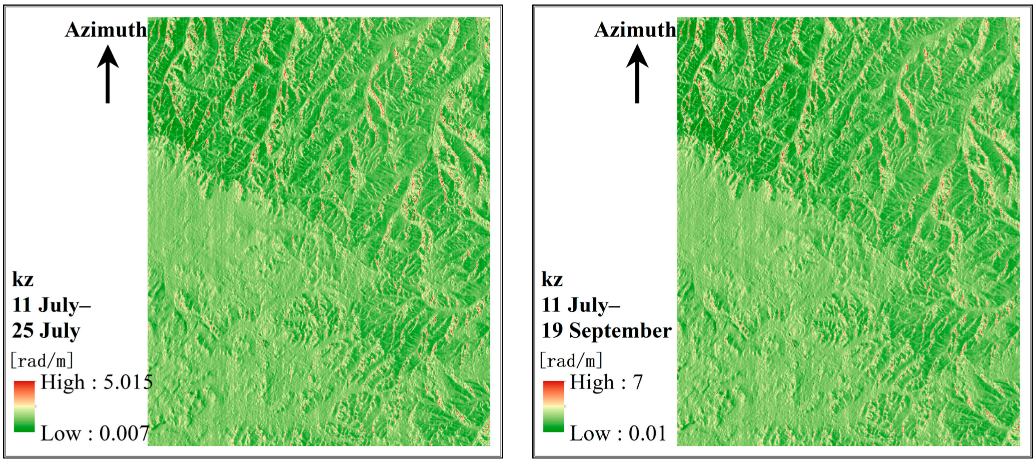

(**a**) (**b**)

Figure 6. Plots of the corrected vertical wavenumber for terrain slope for two interference pairs. (**a**) 11 July–25 July. (**b**) 11 July–19 September.

The conventional ground phase estimation algorithm is optimized using this approach, which focuses on contrast intensity and conflictivity in measurement assessment, as proposed by Diakoulaki [30]. Contrast intensity can be quantified using standard deviation S_n. A higher standard deviation of the complex coherence signifies greater fluctuation and informative content, consequently assigning more weight to enhance the evaluation strength of the respective indicator. The correlation coefficient r_{mn} indicates the conflictiveness of multiple indicators; minimal conflict exists when two coherences exhibit a significantly strong correlation. This subsequently leads to a reduction in the weight assigned to the respective indicator. In order to eliminate the influence of the dimension on the evaluation results, each indicator is dimensionless, and the matrix elements after processing are x'_{mn}.

$$\begin{cases} \overline{x'_n} = \frac{1}{M}\sum_{m=1}^{M} x'_{mn} \\ S_n = \sqrt{\frac{\sum_{m=1}^{M}\left(x'_{mn}-\overline{x'_n}\right)^2}{N-1}} \end{cases}, \tag{7}$$

$$R_n = \sum_{m=1}^{N}(1 - r_{mn}), \tag{8}$$

These two characteristics combined comprise the information C_n. The weight assigned increases with the level of information provided and the importance of nth complex coherence in the overall evaluation indicators system. Consequently, the CRITIC method's objective weights W_n are determined.

$$C_n = S_n \sum_{m=1}^{N}(1 - r_{mn}) = S_n \times R_n, \tag{9}$$

$$W_n = \frac{C_n}{\sum_{n=1}^{N} C_n}, \tag{10}$$

We employed a coherence optimization technique to enhance the degree of complex coherence separation and refined the complex coherence fitting approach. Although coherence straight line fit uses complex coherences such as HH, HV, HH-VV, OPT1, OPT2, and OPT3, they do not fully characterize the shape of the coherence region. This limitation affects the accuracy of ground phase inversion and, consequently, the forest height inversion. In this study, we utilized the coherence region boundary algorithm [31] to acquire polarization vectors (ω_1, ω_2) with maximum separation in the complex plane. By rotating the phase, this method generates multiple pairs of boundary points on the coherence region. The optimal coherence line is determined by connecting the two farthest locations among all extracted boundary points [32]:

$$\begin{cases} T = (T_{11} + T_{22})/2 \\ \Omega = \left(\Omega_{11}e^{i\phi} + \Omega_{22}^{*T}e^{-i\phi}\right)/2 \end{cases}, \tag{11}$$

$$\begin{aligned} & T^{-1}\Omega(\phi)\omega = \lambda(\phi)\omega \\ & \Rightarrow \max_{\phi}|\lambda_{max}(\phi) - \lambda_{min}(\phi)| \\ & \Rightarrow \begin{cases} \lambda_{max} \to \omega_{max} \to \gamma_{max} \\ \lambda_{min} \to \omega_{min} \to \gamma_{min} \end{cases} \end{aligned}, \tag{12}$$

3.3. Iterative Process of Temporal Decorrelation

According to the characteristics of the ALOS-2 (the long temporal baseline and relatively small vertical wavenumber), among many forest height inversion techniques, the multiple iteration method is chosen in this study, which yields the relationship between the observed canopy phases and the actual canopy heights, as seen in Equation (13). Where ε represents the correction term for canopy random motion and the correction term φ_e for the phase center offset. Considering overall coherence, the magnitude term of temporal decoherence $|\gamma_e|$ is introduced, resulting in the final form of the model as given in Equation (14). Figure 7 illustrates a schematic of the interference technique with multiple iterative algorithms.

$$\phi_{vol} = \varepsilon k_z h + \varphi_e, \tag{13}$$

$$\hat{\gamma} = |\gamma_e| \cdot e^{i\varphi_e} \frac{2\sigma}{cos\theta\left(e^{\frac{2\sigma h_v}{cos\theta}} - 1\right)} \int_0^{h_v} e^{-i(\varepsilon \cdot k_z)z} e^{-\frac{2\sigma z}{cos\theta}} dz, \tag{14}$$

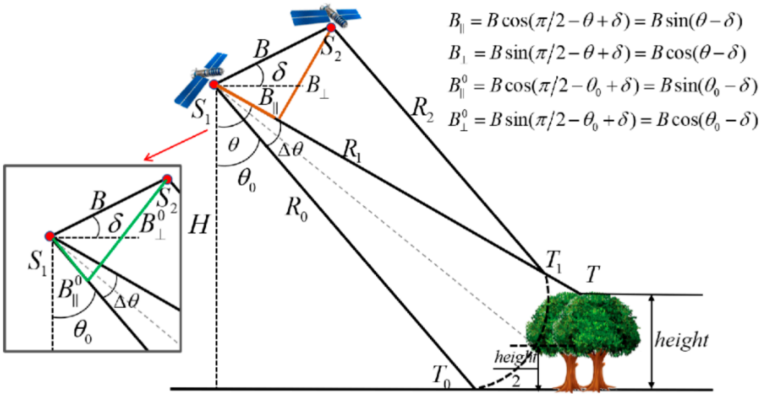

Figure 7. Schematic diagram of the interference technique during phase shift.

This study introduces the concept of mitigating reduced observational coherence by quantifying systematic decoherence γ_{System} instead of $|\gamma_e|$ aiming to enhance the efficiency of the model iteration process. The coherence γ_{Obs} observed by PolInSAR is quantified by the degree of correlation between two complex images: e_1 and e_2 (Equation (15)). γ_{Obs} comprises various independent decoherence mechanisms, with the primary ones under consideration being system decorrelation γ_{System}, temporal decorrelation γ_{Temp}, and volume decorrelation γ_{Vol} [13]. System decorrelation γ_{System} further divides into thermal SNR (signal-to-noise) decorrelation γ_{SNR} arising from sensor antenna characteristics, co-registration decorrelation γ_{Coreg} due to registration errors in interferometric pre-processing, and spatial baseline decorrelation $\gamma_{Baseline}$ [14,33].

$$\gamma_{Obs} = \frac{|\langle e_1 e_2^* \rangle|}{\sqrt{\left\langle |e_1|^2 \right\rangle \left\langle |e_2^*|^2 \right\rangle}}, \tag{15}$$

$$\gamma_{obs} = \gamma_{System}\gamma_{Temp}\gamma_{Vol} = (\gamma_{SNR}\gamma_{Coreg}\gamma_{Baseline})\gamma_{Temp}\gamma_{Vol}, \tag{16}$$

The process involves the removal of systematic decoherence, followed by the minimization of temporal decoherence. Subsequently, the model of temporal decorrelation is employed to deduce the vertical structure of the vegetation. Taking the 11 July–25 July interference pair as an illustration, the SNR is initially computed from metadata. Subsequently, the SNR decoherence is determined using Equation (17), in which $NE\sigma^0$ represents the Noise Equivalent Sigma Naught for normalized backscattering. The calculation involves co-polarization $\gamma_{SNR} = 0.9952$ and cross-polarization $\gamma_{SNR} = 0.9974$, and the one with a greater influence of the SNR, denoted as $\gamma_{SNR} = 0.9952$, is selected.

$$\gamma_{SNR} = \frac{SNR}{1+SNR}, SNR = \frac{\sigma^0}{NE\sigma^0}, \tag{17}$$

The co-registration decorrelation is represented by Equation (18) [34]. The pixel accuracy of the co-registration is consistently within 0.2 pixels for both range-directed δ_{rg} and azimuth-directed δ_{az}, thus obtaining $\gamma_{Coreg} = 0.8751$.

$$\gamma_{Coreg} = \frac{\sin(\pi\delta_{rg})}{\pi\delta_{rg}} \cdot \frac{\sin(\pi\delta_{az})}{\pi\delta_{az}}, \tag{18}$$

Surface scattering gives rise to a notable coherence loss known as baseline decoherence $\gamma_{Baseline}$, expressed as a function of system parameters that include the speed of light c, the perpendicular baseline $B_{\perp}$, bandwidth W, wavelength λ, slant length R, and local incidence θ_{local}, as defined in Equation (19). The computation yields the value $\gamma_{Baseline} = 0.9919$.

$$\gamma_{Baseline} = 1 - \frac{cB_{\perp}}{W\lambda R \tan\theta_{local}}, \tag{19}$$

Multiplying the three decoherences produces the system decoherence $\gamma_{System} = 0.8639$ for the 11 July–25 July interferometric pair and $\gamma_{System} = 0.8601$ the 11 July–19 September interferometric pair. As system decoherence solely impacts coherence amplitude and is phase-independent [35], the observed coherence is normalized by dividing it by the system coherence to acquire the corrected observed coherence.

The corrected observed coherence encompasses volumetric γ_{Vol} and temporal decoherence γ_{Temp}, representing complex factors that influence the observed coherence's magnitude and phase [36]. These factors are the sole remaining coherence components associated with the vertical structure and forest height [37]. In the ALOS-2 data, we modified the multiple iteration algorithm of [18]. Also, we introduced the CRITIC method to improve the ground phase estimation accuracy, resulting in the modified CRITIC-ITDRvoG algorithm as in Equation (20). Figure 8 depicts the inversion flowchart of the PolInSAR algorithm, presenting technical details for both simulated and real datasets.

$$\hat{\gamma} = \gamma_{System} e^{i\varphi_e} \frac{2\sigma}{\cos\theta\left(e^{\frac{2\sigma h_v}{\cos\theta}} - 1\right)} \int_0^{h_v} e^{-i(\varepsilon k_{z0})z} e^{-\frac{2\sigma z}{\cos\theta}} dz, \tag{20}$$

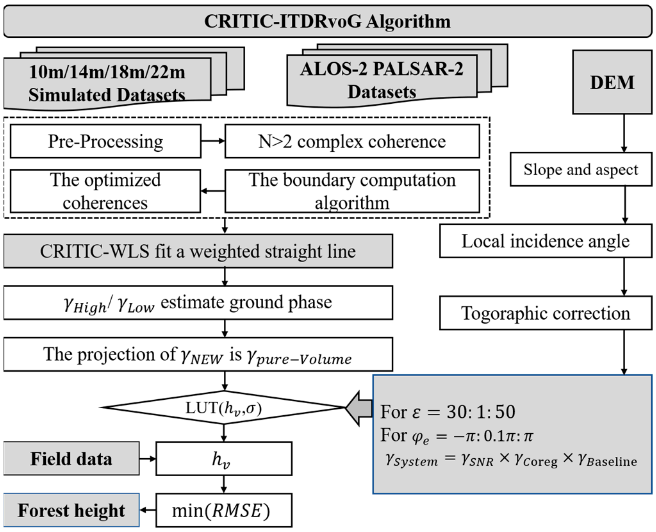

Figure 8. The flowchart illustrates the inversion process of the forest height improvement algorithm proposed in this paper.

4. Results

4.1. Inversion Results for the Simulated Dataset

The CRITIC-WLS algorithm is employed primarily for enhancing the estimation of ground phase and forest height, given that the simulated dataset is devoid of influences from terrain slope and temporal decoherence. A comparative analysis is conducted between the ground phase and forest height results derived from the CRITIC-WLS algorithm and those obtained using the conventional three-stage algorithm.

4.1.1. Results of Ground Phase Estimation

The actual ground phase of the simulated dataset is 0 rad. Figure 9a–d illustrate and compare the ground phase and accuracy of the two methods, respectively. Compared to the original algorithm, the optimized approach demonstrates significantly higher accuracy in both ground phase inversion and overall accuracy. The method consistently reduces the ground phase estimation error across forest height–density datasets.

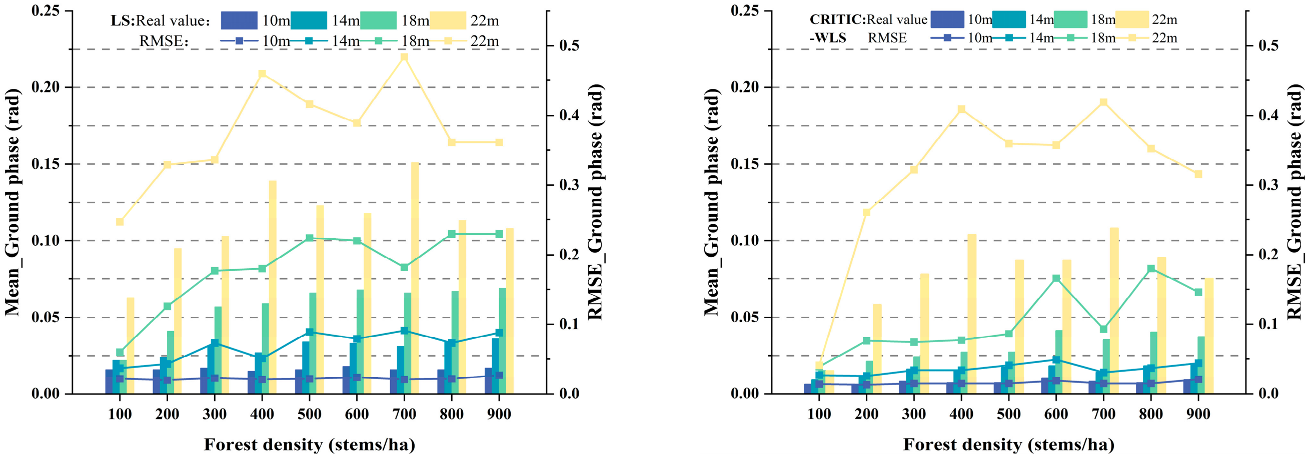

(**a**) LS forest height inversion results and RMSE (**b**) CRITIC-WLS forest height inversion results and RMSE

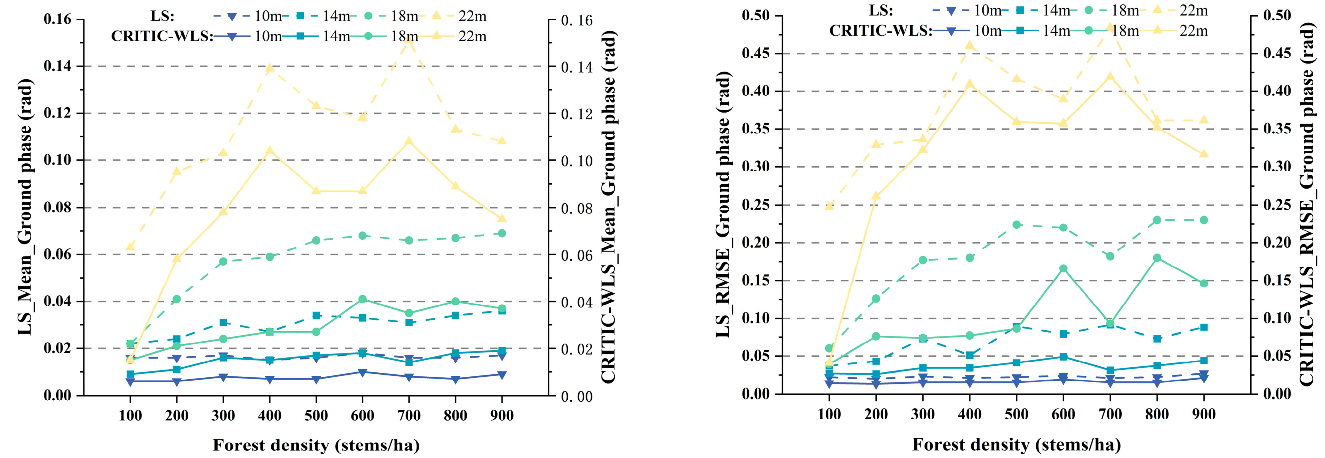

(**c**) Line graph of the forest height for both algorithms (**d**) Line graph of the forest height RMSE for both algorithms

Figure 9. (**a**) Histogram of the average ground phase and a line graph of RMSE for the original algorithm; (**b**) histogram of the average ground phase and a line graph of RMSE for the improved algorithm; (**c**) line graph of the ground phase for both algorithms; (**d**) line graph of the ground phase RMSE for both algorithms.

The enhanced algorithm's inversion progressively increased the ground phase at lower forest heights (10 m/14 m) without reaching a saturation point. The estimation results consistently remained within 0.02 rad, and the RMSE continuously measured below 0.05 rad, indicating superior performance compared to the conventional algorithm. Notably, the ground phase now exhibits less sensitivity to the forest density.

The accuracy of ground phase estimation declines as the range of ground phase change increases due to rising forest density at high forest heights (18 m/22 m). When the forest height is 18 m, the ground phase of the improved algorithm stays within 0.04 rad, while the ground phase result of the traditional algorithm exceeds 0.04 rad at 300 stems/ha, which indicates that the improved algorithm can significantly improve the inversion performance. Despite the ground phase reaching a saturation point at 400 stems/ha both before and after the improvement, the improved algorithm significantly enhances the accuracy of ground phase estimation by 0.05 rad at a 22 m forest height. Consequently, the primary determinant impacting ground phase estimation accuracy is the variation in forest height, with forest density exerting a secondary influence. The higher the forest height, the lower the ground phase estimate accuracy, causing the ground phase saturation point to occur at a lower forest density.

4.1.2. Results of Forest Height Estimation

The average forest height and inversion accuracy of the simulated datasets for each height type are presented in Figure 10a–d. Overall, the optimized algorithm demonstrates superior inversion accuracy to the original algorithm. The application of the RVoG model in scenarios involving 10 m 100 stems/ha and 10 m 200 stems/ha forests faces challenges due to their low and sparse nature, resulting in irregular changes in complex coherence. The RVoG model currently has this issue. Notably, the optimization algorithm exhibits stability, as evidenced by the improvement in the RMSE of forest height across various height–density datasets.

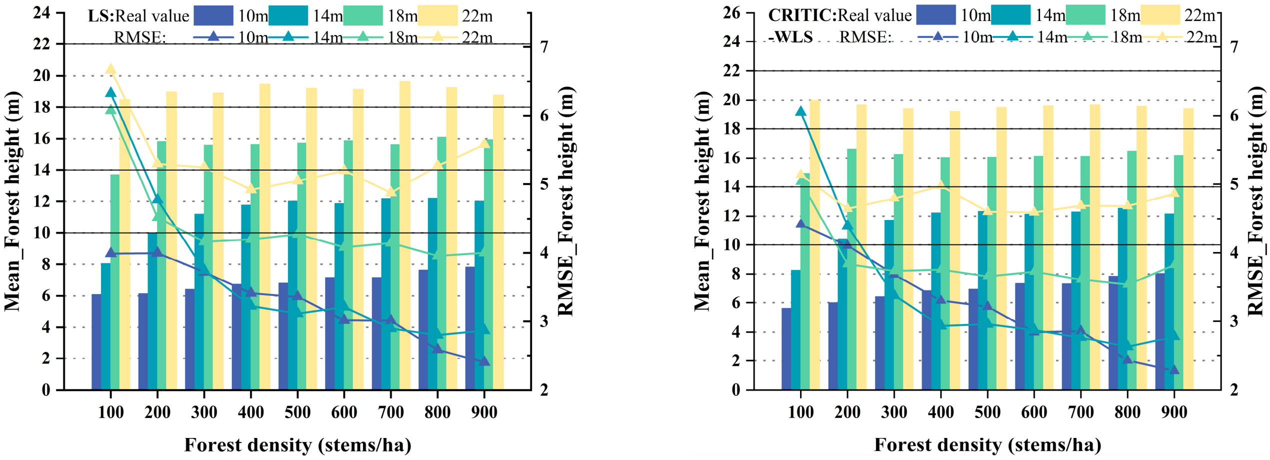

(**a**) LS forest height inversion results and RMSE (**b**) CRITIC-WLS forest height inversion results and RMSE

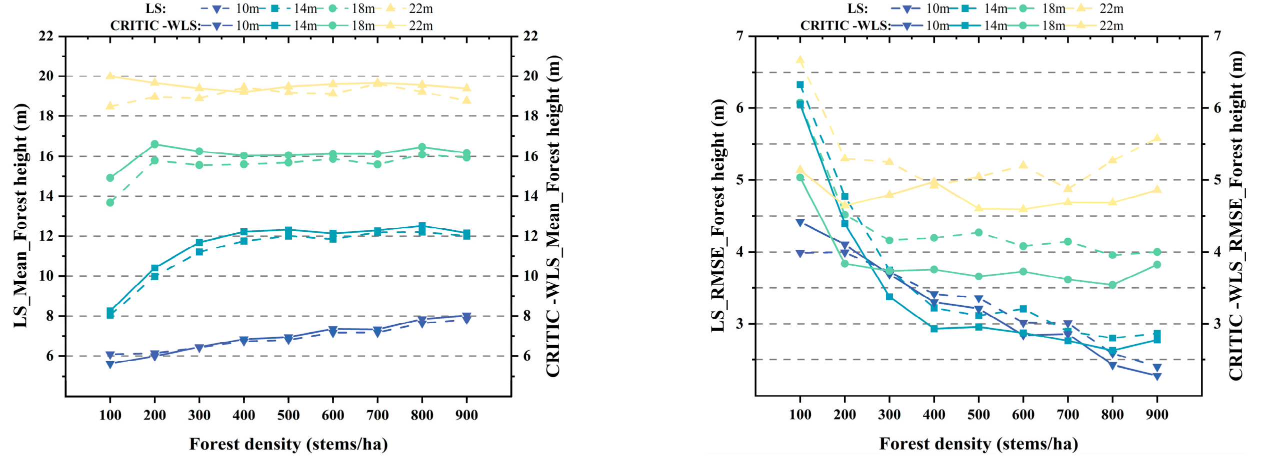

(**c**) Line graph of the forest height for both algorithms (**d**) Line graph of the forest height RMSE for both algorithms

Figure 10. (**a**) Histogram of the average forest height and line graph of RMSE for the original algorithm; (**b**) histogram of the average forest height and line graph of RMSE for the improved algorithm; (**c**) line graph of the forest height for both algorithms; (**d**) line graph of the forest height RMSE for both algorithms.

In the low stand scenario, with the increase in forest density, the inversion results of forest height gradually increased. Additionally, the corresponding RMSE gradually decreased, and the saturation point of forest height also gradually appeared: this trend was especially obvious in the 14 m dataset. The saturation point of forest height appeared earlier in taller stands, and the increasing trend of forest height was no longer obvious with the increase in forest density. Overall, the accuracy of the optimized algorithm for inversion of forest height was improved by 0.5 m compared with the traditional algorithm, and the optimized algorithm was effective in reducing the RMSE of forest height. Table 4 showed the MAPE of two tree height models, and the accuracy of the improved model was better than that of the traditional algorithm, indicating that the optimized ground phase had a significant effect on improving the accuracy of the inversion of forest height.

Table 4. Accuracy of forest height MAPE (%) for four dataset groups.

Forest Density (stems/ha)	**100**	**200**	**300**	**400**	**500**	**600**	**700**	**800**	**900**
				10 m forest height MAPE (%)					
LS	39.17	38.67	35.89	32.70	31.97	28.36	28.32	23.67	21.84
CRITIC-WLS	56.48	40.12	35.66	31.56	30.52	26.57	26.77	21.56	19.76
				14 m forest height MAPE (%)					
LS	42.54	29.03	21.33	17.24	15.70	16.90	14.93	14.18	15.34
CRITIC-WLS	41.07	25.99	18.19	14.31	14.30	14.99	14.06	12.96	14.40
				18 m forest height MAPE (%)					
LS	26.05	17.59	15.64	14.56	16.13	15.25	15.98	14.29	15.03
CRITIC-WLS	20.33	14.39	13.45	13.56	13.90	13.79	13.72	12.66	14.62
				22 m forest height MAPE (%)					
LS	21.20	16.47	16.54	15.74	15.26	15.89	14.83	15.66	17.22
CRITIC-WLS	15.75	13.99	15.26	14.78	14.43	14.33	14.44	14.33	15.49

4.2. Inversion Results for the Real Dataset

In this study, a ratio of 1:2 was employed for the number of test and validation sets, comprising 24 sample plots in the test set and 48 sample plots in the validation set. The datasets 11 July–25 July and 11 July–19 September had parameters that were iterated using the test set data. The flowchart (Figure 11) displays the specific iteration parameters. In this instance, a canopy random motion compensation term ranging from 20 to 40 is applied, guided by a priori conclusions drawn from the literature [31]. However, this study enhances the multiple iteration algorithm proposed by [31]: instead of specifying the coherence amplitude iteration term, we introduce quantized system decoherence. Simultaneously, the initial value of the canopy random motion compensation term is increased, set between 30 and 50. This approach substitutes the system decoherence and a higher canopy random motion compensation term for the coherence amplitude iteration term in the original model, thereby enhancing the efficiency of the multiple iteration procedure.

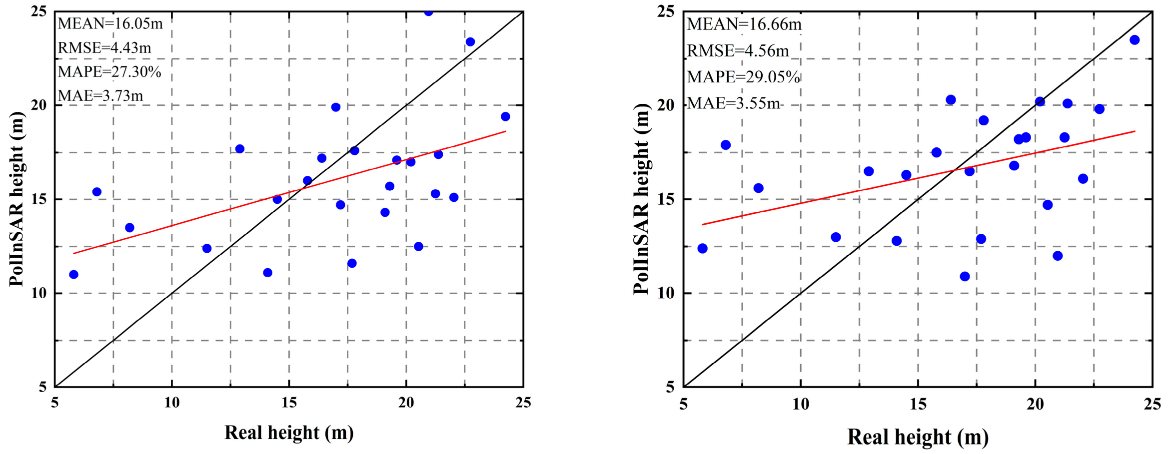

(**a**) (**b**)

Figure 11. Scatterplot of test set inversion results. Blue dots represent sample points, red lines represent fitted lines, and black lines represent 1:1 lines. (**a**) 11 July–25 July. (**b**) 11 July–19 September.

After iteration, the improved model obtains the corresponding phase offset term and the vertical wavenumber by introducing the vertical wavenumber with pixel-by-pixel correction, the CRITIC-WLS ground phase estimation method, and the system decoherence. The specific parameters are displayed in Table 5. Root mean square error (RMSE), mean absolute percentage error (MAPE), and mean absolute error (MAE) for both the validation and test sets are computed by applying the empirical parameters to the two validation sets, as indicated in Table 5.

Table 5. Iteration parameters and inversion accuracy results for two sets of interference pairs. The inversion accuracy includes the accuracy results of the test and validation sets.

Datasets	φ_e	Average Suitable k_z	RMSE (m)	MAPE (%)	MAE (m)
11 July–25 July	$e^{i \cdot 0.94\pi}$	0.43	4.43/2.27	27.30/11.33	3.73/1.84
11 July–19 September	$e^{i \cdot 2.83\pi}$	0.70	4.56/2.59	29.05/11.56	3.55/1.86

Table 5 illustrates the enhanced model's superior performance in reducing the impacts of temporal decoherence. This is evidenced by the accuracy of both test and validation sets exceeding 80%, the validation set's RMSE being approximately 2.5 m, and the MAE being less than 2 m. Notably, the long-term baseline dataset's inversion accuracy is improved, suggesting the enhanced technique is robust. Figures 11 and 12 present scatterplots for the test and validation sets, respectively.

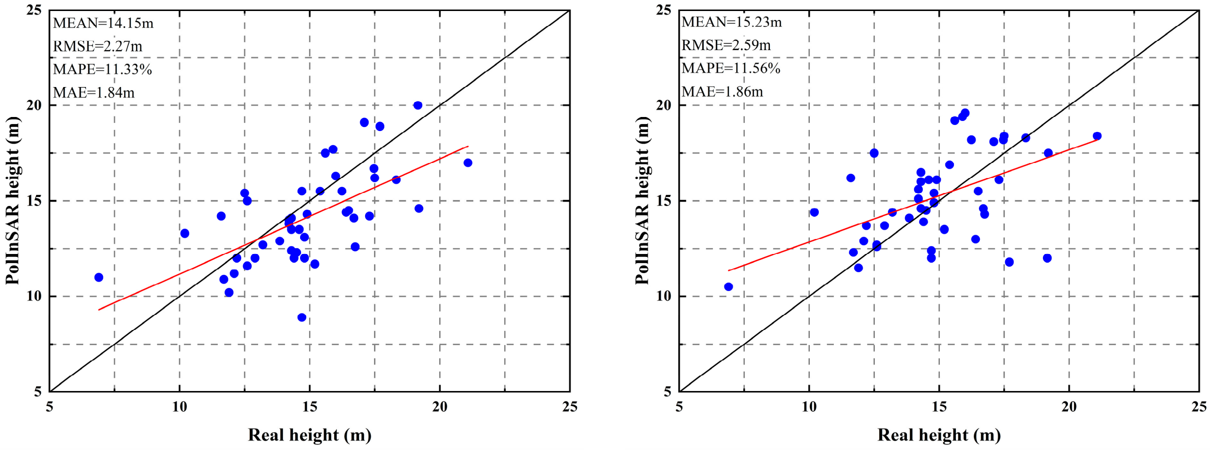

(**a**) (**b**)

Figure 12. Scatterplot of validation set inversion results. Blue dots represent sample points, red lines represent fitted lines, and black lines represent 1:1 lines. (**a**) 11 July–25 July. (**b**) 11 July–19 September.

5. Discussion

5.1. Discussion of the Ground Phase

When transformed by the vertical wavenumber, the ideal scenario entails the interferometric phase difference between topography and canopy equivalent to the forest height. In practical terms, however, with increasing forest height, the ground phase shifts from the surface, causing a concurrent rise in coherence phase height, as illustrated in Figure 13a. A phase difference arises, not corresponding directly to the vegetation height, due to the shift of the canopy phase center away from the top of the canopy caused by electromagnetic wave penetration. The penetration capability of electromagnetic waves diminishes with increasing forest density, resulting in a saturation phenomenon in the coherence phase. Conversely, as forest density decreases, electromagnetic wave penetration capability increases, reducing the phase difference between the ground and canopy and increasing the error of the associated vegetation height. This observation underscores the necessity to assess the impact of more precise ground phase compensation on the accuracy of forest height measurements.

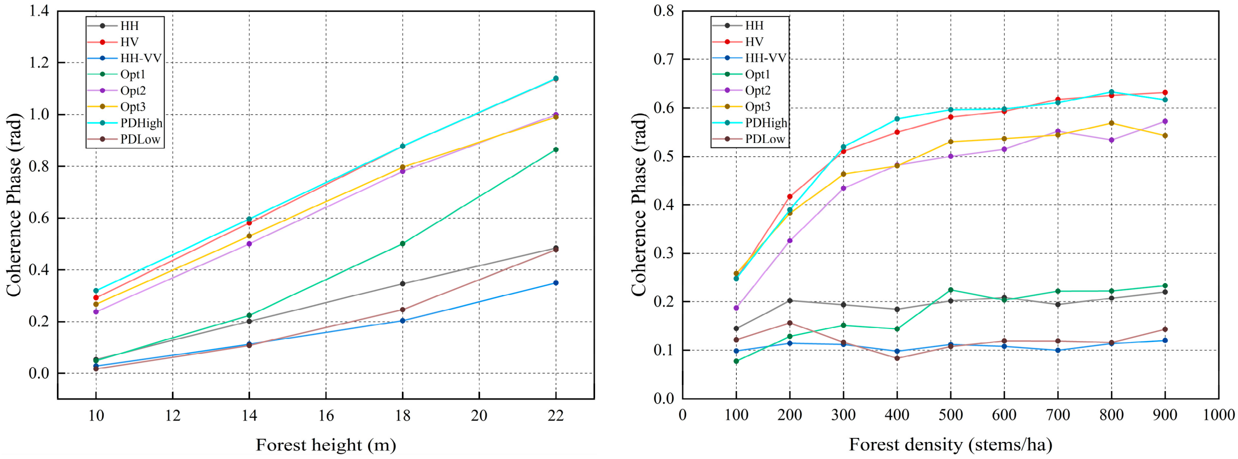

(**a**) (**b**)

Figure 13. Relationship of coherence phase with forest height and forest density. (**a**) Fixed forest density of 500 stems/ha, plot of coherence phase versus forest height for usual polarizations. (**b**) Fixed forest height of 14 m, plot of coherence phase versus forest density for usual polarizations.

5.2. Discussion of Errors in Forest Heights

With polarization, dependence, ground, and canopy contributions can influence the ground-to-volume scattering ratio (GVR). In Figure 14a, as forest height grows, the GVRs of the ground scattering and volume scattering gradually decline and rise, respectively. The phase center of each polarization rises with increasing forest height (Figure 13a), the corresponding ground phase center increasingly deviates from the actual ground position, and the GVR, which represents the ground scattering, diminishes as the forest height rises. The distance between the ground and the canopy's polarization centers increases significantly with forest height (Figure 13a), which causes a corresponding increase in the GVR that represents scattering from the volume (Figure 14a).

$$GVR(\omega) = \frac{abs(\gamma_{V-assu} - \gamma_{Obs}(\omega))}{abs(\gamma_{Obs}(\omega) - \exp(i\phi_{ground}))}, \tag{21}$$

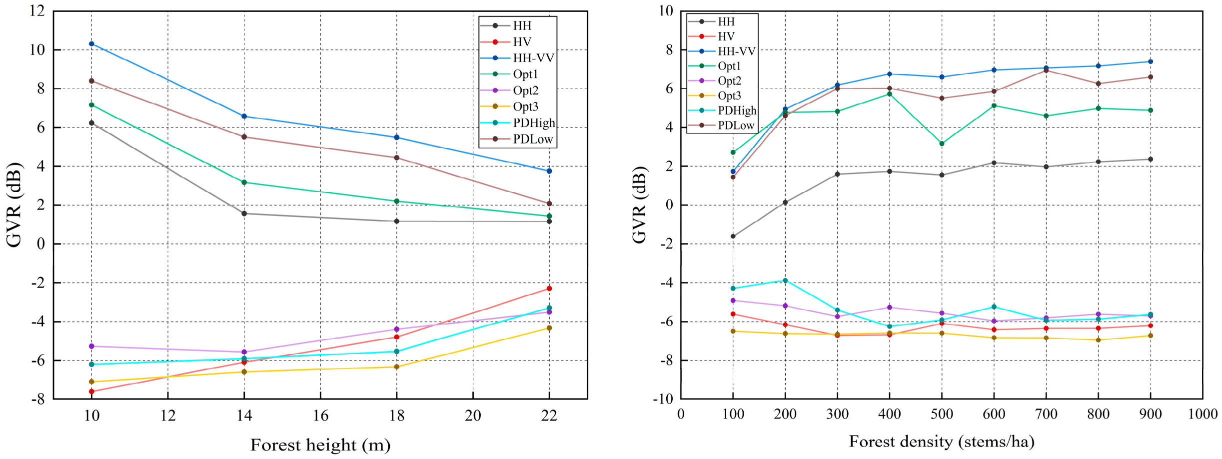

(**a**) (**b**)

Figure 14. Ground-to-volume scattering ratio (GVR) versus forest height and forest density. (**a**) Fixed forest density of 500 stems/ha, plot of GVRs versus forest height for usual polarizations. (**b**) Fixed forest height of 14 m, plot of GVRs versus forest density for usual polarizations.

As illustrated in Figure 14b, an increase in forest density leads to a gradual reduction in the GVR representing volume scattering, while the GVR reflecting ground scattering shows a corresponding increase. This observation aligns with the conclusions of [36], as stronger ground echoes in areas with sparser vegetation allow the electromagnetic wave to reach the surface more easily. Conversely, with a higher density of the forest stand, stronger canopy echoes decrease the GVR associated with volume scattering.

The GVR of HV/PDHigh polarization, indicative of canopy scattering, was consistently lower than that of HH-VV/PDLow polarization, representing ground scattering across varying forest heights and densities. Representative volume scattering's GVR demonstrated a positive correlation with forest height and an inverse relationship with forest density. If the accuracy of the three-stage algorithm is less than 10%, the minimum GVR of the volume scattering should be less than −10 dB. However, this study's observed minimum GVR values under different forest heights and densities slightly exceed −10 dB. Consequently, GVR variations also impact the inversion outcomes of the improved algorithm.

5.3. Limitations of the CRITIC-WLS Ground Phase Improvement Algorithm

The improved methodology exhibits limitations in its applicability to low, sparse forests, which is consistent with findings reported in other implementations of the RVoG model [36]. This constraint arises due to the non-uniformity of complex coherence variations in low, sparse environments and the heterogeneous structure of the forest, deviating from the assumptions inherent in RVoG model applications. These assumptions include uniform mean extinction for all polarizations, a homogeneous layer of randomly oriented vegetation particles, and an impenetrable ground. In specific instances, there is nearly equal coherence among all polarizations, notably between the HH-VV polarization of the ground and the HV polarization representing the canopy in scenarios with forest densities of 10 m 100 stems/ha and 10 m 200 stems/ha, as depicted in Figure 15. The reason for this occurrence is that when forest density and forest height increase, volume coherence decreases. The volume decoherence of low and sparse forests is weak, and the coherence difference of different polarization is not significant in low and sparse forests. This especially happens when the SNR decoherence dominates the phase error. Addressing SNR decoherence in low and sparse forest settings has the potential to enhance inversion performance.

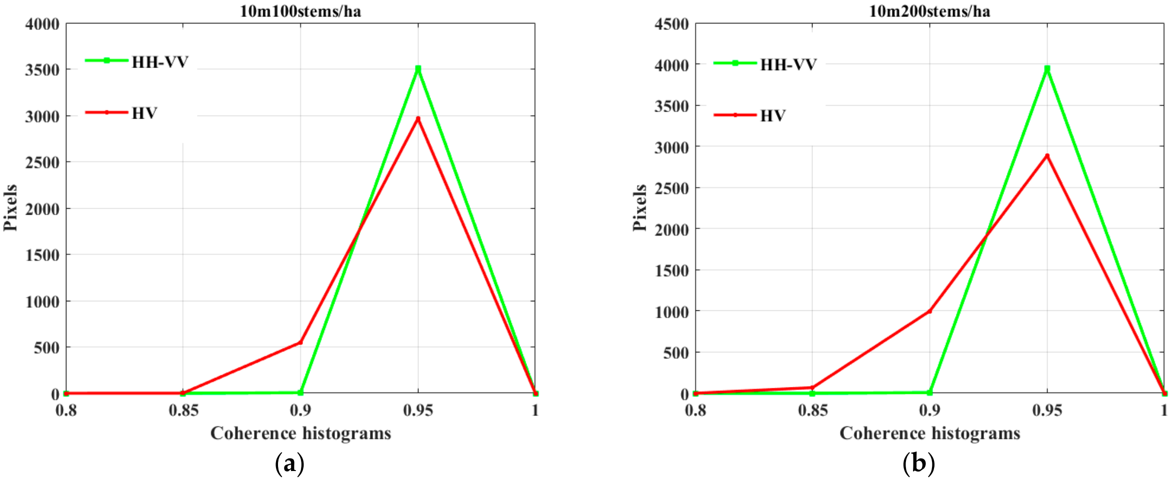

(**a**) (**b**)

Figure 15. Coherence histogram of HH-VV polarization and HV polarization for (**a**) 10 m 100 stems/ha and (**b**) 10 m 200 stems/ha.

Similar complex coherences arise due to the effective penetration of electromagnetic waves through the canopy in areas characterized by lower and sparse vegetation. As depicted by the black and red ellipses in Figure 16, there is less separation of the complex coherence in the low, sparse forest (10 m 100 stems/ha) than in the tall, dense forest (14 m 500 stems/ha). A geometric parameter known as the "narrowness ratio" is introduced to quantify this observation. This ratio represents the relationship between the long and short axes of the coherence ellipse and was initially introduced in the literature of [18]. The ground phase estimation error decreases as the narrowness ratio decreases, bringing the results closer to the actual forest. Notably, low, sparse forests exhibit a larger narrowness ratio, resulting in elevated errors in topographic estimation. Under low, sparse forest conditions, specifically at 10 m 100 stems/ha and 10 m 200 stems/ha, combining these two factors leads to the poor inversion effects of the CRITIC improved algorithm.

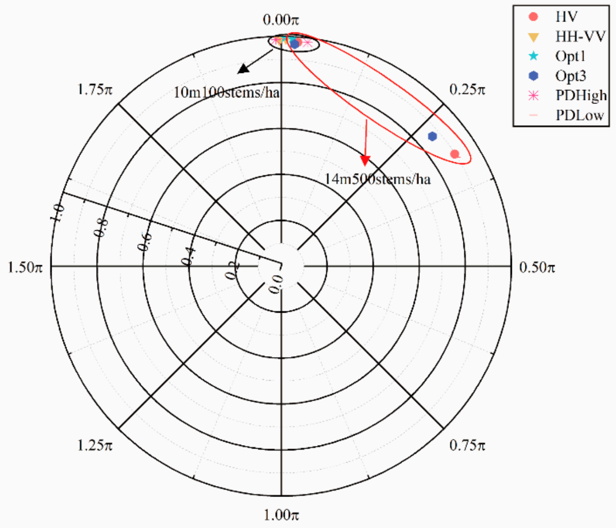

Figure 16. The shape of the coherence area of low and sparse forests.

5.4. Discussion of the CRITIC-ITDRvoG Algorithm

The extraction of the terrain-corrected vertical wave number for each pixel, a feature also integrated into the iterative model, represents a notable enhancement over the original model employed in this study. The precision of topographical information is evident in the inversion result maps of forest height in the Saihanba for both datasets, as illustrated in Figure A4. In contrast to the original model, which utilized a single average vertical wave value for the entire map, the improved model provides a more detailed consideration of the terrain effects on each pixel.

While valuable, the conclusion drawn in [31] is not directly applicable to this study. Our improved algorithm incorporates the enhanced canopy random motion phase offset term, system decoherence, and phase error term resulting from SAR penetration of the canopy. However, it does not explicitly define a coherence amplitude iteration term value. The research findings indicate a substantial increase in phase offset and error terms as the temporal baseline extends. Illustrated in Figure 17 are the phase frequency histograms and diagrams for the two datasets. In the 11 July–19 September dataset, it is observed that the phase values are lower, and there is a uniform and reduced overall frequency of interference phase occurrences. This narrowing of the phase gap adversely affects the fitting of the complex coherence straight line compared to the dataset with a shorter time baseline. Table 6 presents the mean, standard deviation, and variance of the HV-polarized interferometric phases for each interferometric pair. Larger standard deviation and variance values for the 11 July–25 July data suggest a more dispersed and discrepant phase distribution for this interferometric pair. Conversely, the long-time baseline 11 July–19 September dataset, influenced by greater temporal decoherence, exhibits a lower phase that is typically less varied and discrepant. Consequently, the 11 July–19 September dataset requires a higher phase compensation term than the 11 July–25 July dataset.

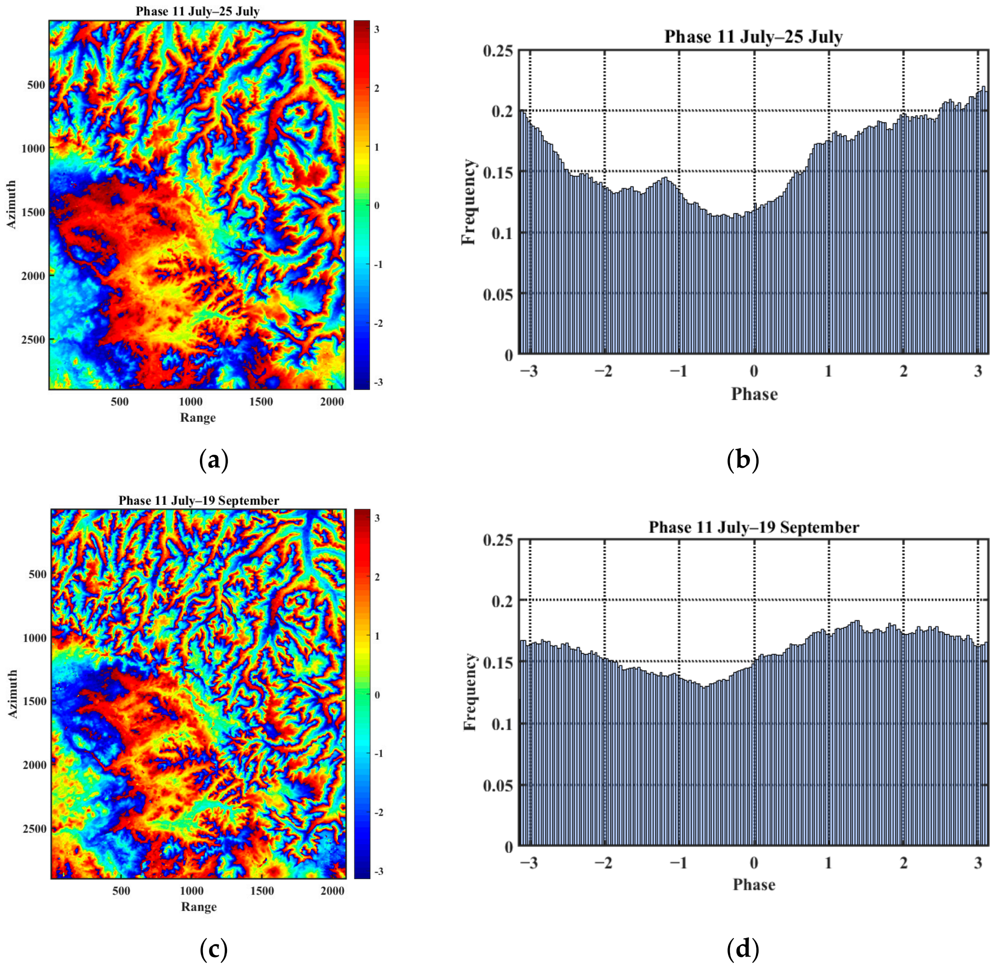

(**a**) (**b**)

(**c**) (**d**)

Figure 17. Phase graphs and phase frequency histograms of HV polarization for both datasets. (**a**) Phase graphs for 11 July–25 July. (**b**) Phase frequency histograms for 11 July–25 July. (**c**) Phase graphs for 11 July–19 September. (**d**) Phase frequency histograms for 11 July–19 September.

Table 6. Statistical parameters of HV interference phases for two datasets.

Datasets	Average of HV Phases	Variance of HV Phase	The Standard Deviation of HV Phase
11 July–25 July	0.2004	3.6603	1.9132
11 July–19 September	0.0909	3.3908	1.8419

While the improved model demonstrates enhanced inversion accuracy, it is acknowledged that the coherence amplitude diminishes with the increase in time baseline. However, the proposition in this study is that the system decoherence and canopy random motion term may compensate for the shift in coherence amplitude. Figure 18 illustrates the coherence amplitude frequency histograms and HV-polarized amplitude plots for the interference pairs 11 July–25 July and 11 July–19 September. The coherence amplitude of the dataset with a longer time baseline is approximately 0.2, which is smaller than that of the dataset with a shorter time baseline. This study attributes this difference to meteorological variations, particularly differences in wind speed and seasonal changes. Figure 5 indicates that there was no rainfall during the data collection on 11 July and 25 July, highlighting wind speed fluctuations as the primary factor influencing the random movement of the canopy. The 70-day interval between the collection time of the 19 September slave image and the master image, along with the lowest temperature of 2.1 °C on the day of image collection on 19 September and the commencement of the forest defoliation season in the study area, characterized by high wind speeds, collectively contributed to a reduction in the amplitude of the 11 July–19 September dataset. In this interferometric pair, the decrease in amplitude necessitated more significant compensation for random motion. Additionally, rainfall on 16 September and subsequent dielectric constant variations influenced this sample's phase correction term.

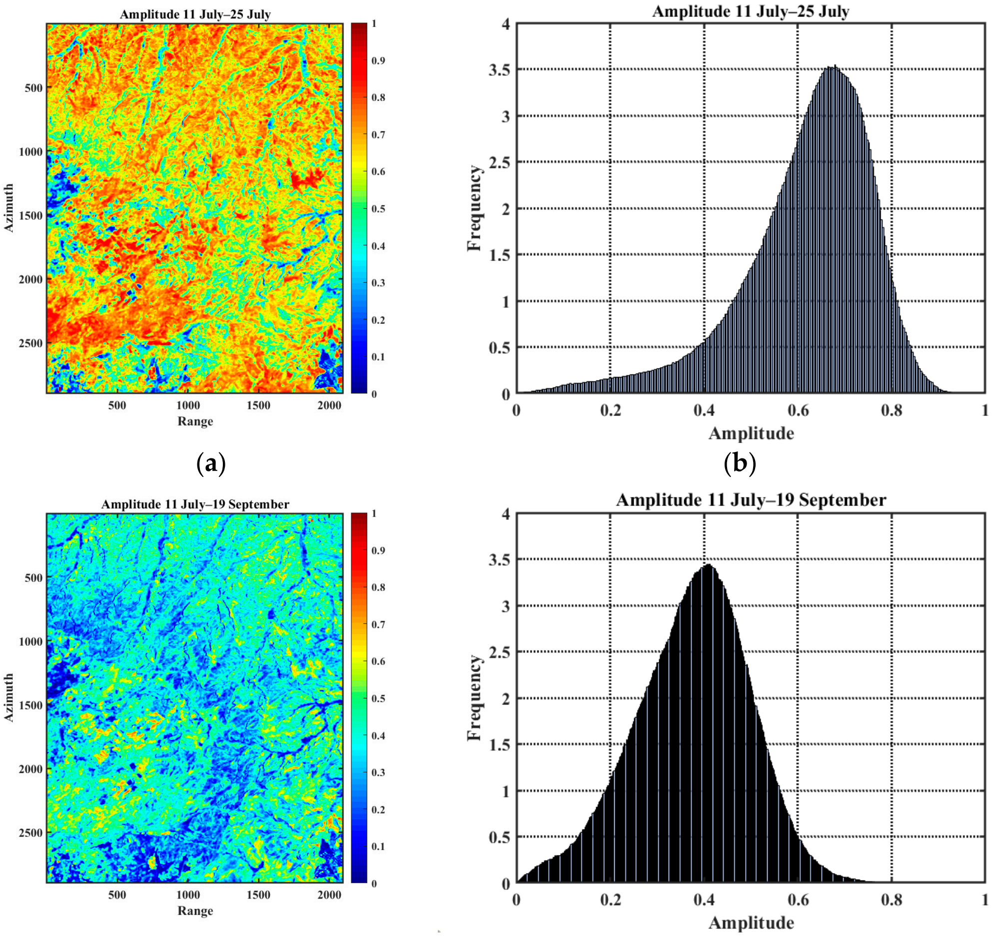

(**a**) (**b**)

(**c**) (**d**)

Figure 18. Coherence amplitude graphs and frequency histograms of HV polarization for both datasets. (**a**) Coherence amplitude graphs for 11 July–25 July. (**b**) Coherence amplitude frequency histograms for 11 July–25 July. (**c**) Coherence amplitude graphs for 11 July–19 September. (**d**) Coherence amplitude frequency histograms for 11 July–19 September.

Figure 19 illustrates the configurations of coherence regions for two ALOS-2 interferometric pairings within the same pixel. A red dashed ellipse denotes the tall forest stand at 21.9 m, while a green dashed ellipse represents the low forest stand at 12.9 m. Additionally, we present the configurations of coherence regions for simulated datasets with average tree heights of 14 m (depicted by the green solid ellipse) and 22 m (represented by the black solid ellipse). This comparative study aims to assess the impact of temporal decoherence on the polarization interferometric dataset. We observe that, in the absence of temporal decoherence interference (simulated dataset), the long axis of the coherence ellipse is slightly larger in tall stands compared to low stands. Notably, the coherence phases of different complex coherences exhibit variations, and the coherence magnitude is slightly smaller in tall stands than in low stands. However, in the case of the ALOS-2 dataset under temporal decoherence interference, both the coherence amplitudes and coherence phases of the two interfering pairs decrease with the increase in the temporal baseline for both tall and low forest stands. Within an image pixel, the variability of complex coherence phases diminishes as the coherence amplitude approaches the origin of the complex unit circle.

Notably, in low stands, both the coherence amplitude and coherence phase experience a reduction of more than half, highlighting the significant impact of temporal decoherence, which is more pronounced in low stands compared to taller stands. For instance, as the temporal baseline extends from 14 to 70 days for a forest height of 12.9 m, the amplitude of HV polarization diminishes from 0.4 to 0.1 and the coherence phase declines from $exp(i \cdot \pi)$ to $exp(i \cdot 1.65\pi)$. Building upon the preceding discussion, in a physical context, this implies that the phase center of HV polarization in the canopy is higher for the 11 July–19 September dataset (70-day temporal baseline) than the 11 July–25 July dataset (14-day temporal baseline). Hence, a larger correction parameter is employed to manage this error term, considering both the number of vertical wavenumbers and random motions within the canopy. Consequently, the inversion of the 11 July–25 July dataset demonstrates higher accuracy than the 11 July–19 September dataset, which tends to be overestimated and exhibits a larger iteratively corrected vertical wavenumber than the former.

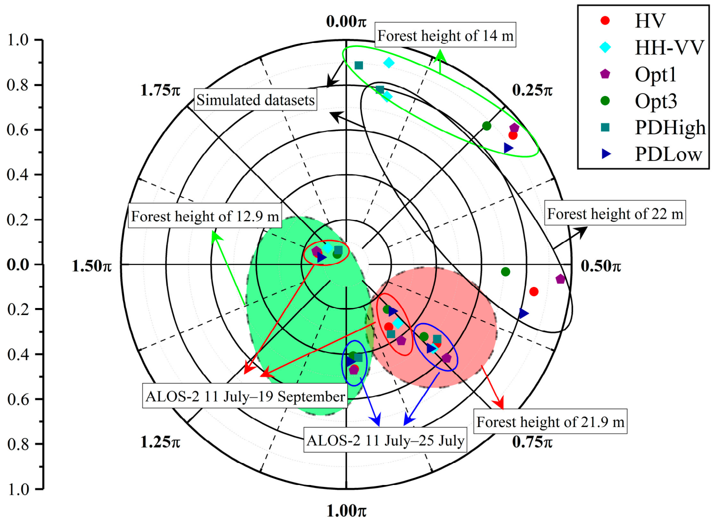

Figure 19. The shape of the coherence region is depicted for both the simulated dataset and the ALOS-2 dataset, considering tall and low forest stands. In the ALOS-2 images, the green dashed ellipse corresponds to an average tree height of 12.9 m, while the red dashed ellipse represents an average tree height of 21.9 m. In the simulated data images, the green solid ellipse signifies an average tree height of 14 m, and the black solid ellipse represents an average tree height of 22 m.

6. Conclusions

This study enhances the first stage of the conventional three-stage model by integrating the CRITIC weighted least squares model to estimate the ground phase, leading to improved ground phase estimation and forest height inversion accuracy. This methodology achieves a more accurate ground phase estimate by reducing the weights of indicators containing redundant data. However, it is essential to note that the application of the enhanced algorithm in lower and sparse-scene scenarios remains constrained. In low, sparse forest scenarios, on the one hand, the coherence of polarizations representing both the ground and the canopy is nearly identical. Despite enhanced accuracy in ground phase estimation, distinguishing the canopy–ground phase in this context remains challenging due to the narrow width of the coherence ellipse.

This study further elucidates that forest height rather than density is the primary factor influencing ground phase estimation errors. An excessively high stand density saturates the ground phase, diminishing the ability to distinguish the canopy from the ground. Volume scattering's GVR demonstrated a positive correlation with forest height and an inverse relationship with forest density. Both forest height and density affect the GVR. The residual ground contribution in the volume scattering channel also affects the inversion accuracy of the improved algorithm. In the next stage, we combine the CRITIC-weighted method for estimating ground phase with coherence magnitude and the three-stage hybrid iterative application model [20] for whole stand density. We explore whether the improved model can reduce the interference of forest structure to the model.

Furthermore, we employ this CRITIC-weighted method with the iterative temporal decoherence algorithm on the L-band ALOS-2 PALSAR satellite datasets, characterized by varying temporal baselines. The inversion accuracies for both datasets exceed 80%, with errors consistently within 2 m, attesting to the remarkable accuracy and robustness of the algorithm. Concurrently, we observed that temporal decoherence induces attenuation in both phase and amplitude, particularly affecting shorter stands to a greater extent than taller ones. When dealing with larger temporal baseline datasets, compensatory terms for canopy random motion and phase offset become more substantial to mitigate the risk of overestimating tree height inversion. Furthermore, the inherent instability stemming from temperature, wind, and precipitation variations during data collection exacerbates the impact of temporal decoherence, which is particularly pronounced in large temporal baseline datasets.

This study proposes an optimization method for improving the accuracy of ground phase and correcting temporal decoherence. The effects of ground phase on forest height and forest density and the error sources affecting the inversion of stand height were analyzed. At the same time, the source of temporal decoherence, the qualitative law of temporal decoherence and forest height, phase, and amplitude, are given, which also lays a foundation for finding the quantitative relationship between these SAR parameters and forest structure parameters in the future.

Author Contributions: Conceptualization, W.F. and A.S.; methodology, software, validation, and writing—original draft preparation, A.S.; formal analysis, A.S.; writing—review and editing, A.S. and W.F. All authors have read and agreed to the published version of the manuscript.

Funding: This research was funded by the National Natural Science Foundation of China (contract no. 31971654) and the Civil Aerospace Technology Advance Research Project (contract no. D040114).

Data Availability Statement: Data are contained within the article.

Conflicts of Interest: The authors declare no conflicts of interest.

Appendix A

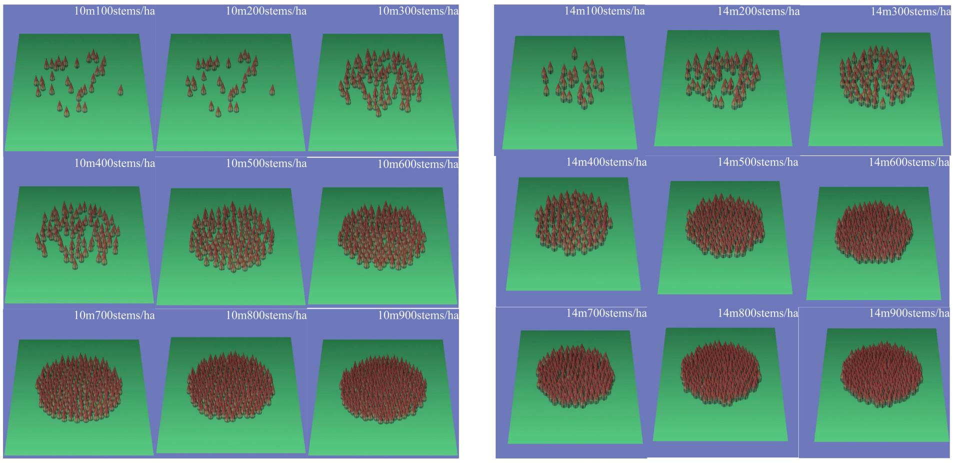

(**a**) (**b**)

Figure A1. *Cont.*

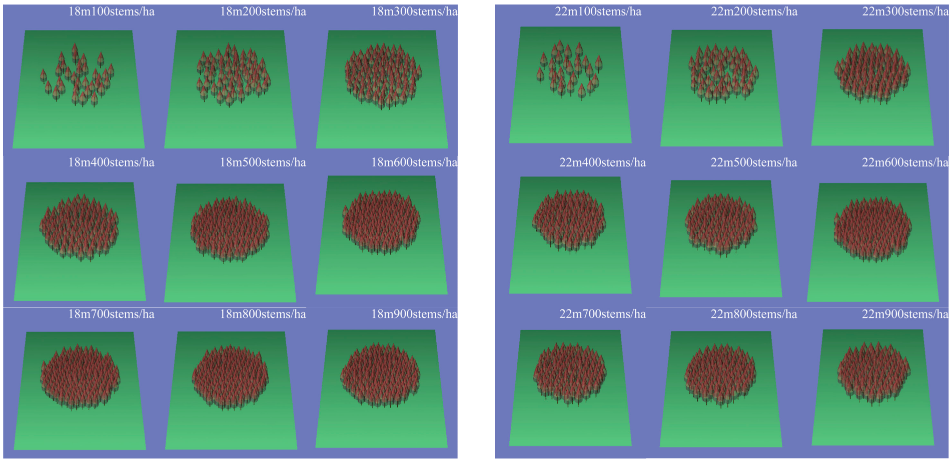

(**c**) (**d**)

Figure A1. Scenarios represent four different types of simulated data. (**a**) 10 m. (**b**) 14 m. (**c**) 18 m. (**d**) 22 m.

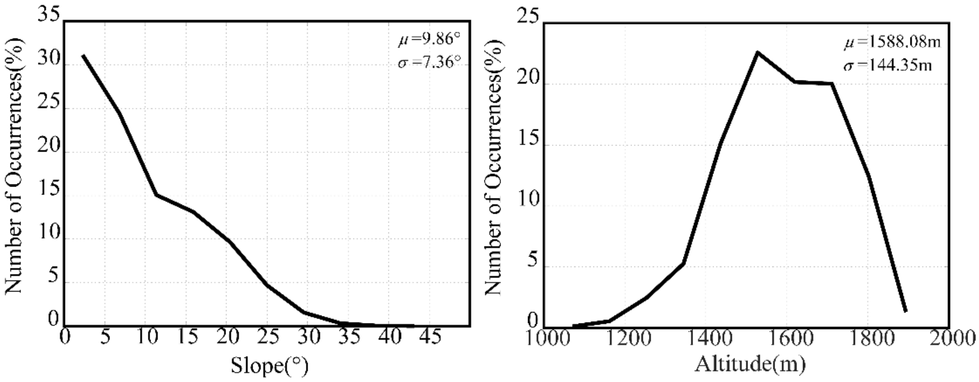

Figure A2. The distribution of slope (on the **left**) and elevation (on the **right**) in the study area is presented with the mean (μ) and the standard deviation (σ) of slope and elevation.

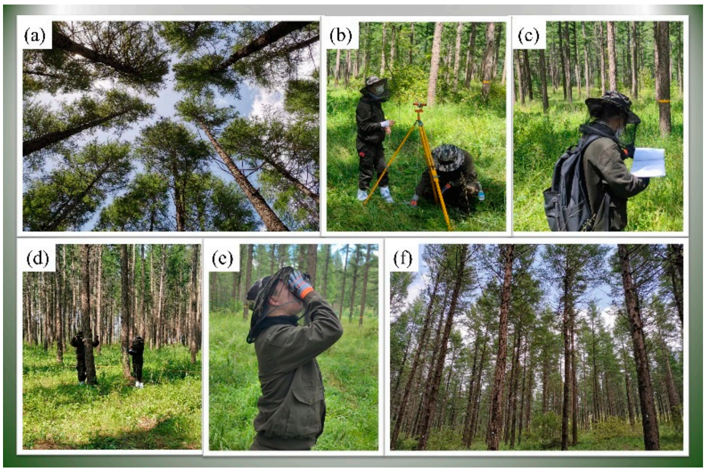

Figure A3. Situation of the forest in the study region and details of field measurements. (**a**,**f**): representative larch forest state in the study area; (**b**,**c**): measurements at standard plot boundaries and recording of sample plot coordinates; (**d**): diameter at breast height (DBH) measurements for each tree in the sample plot; (**e**): height measurements for each tree in the sample plot.

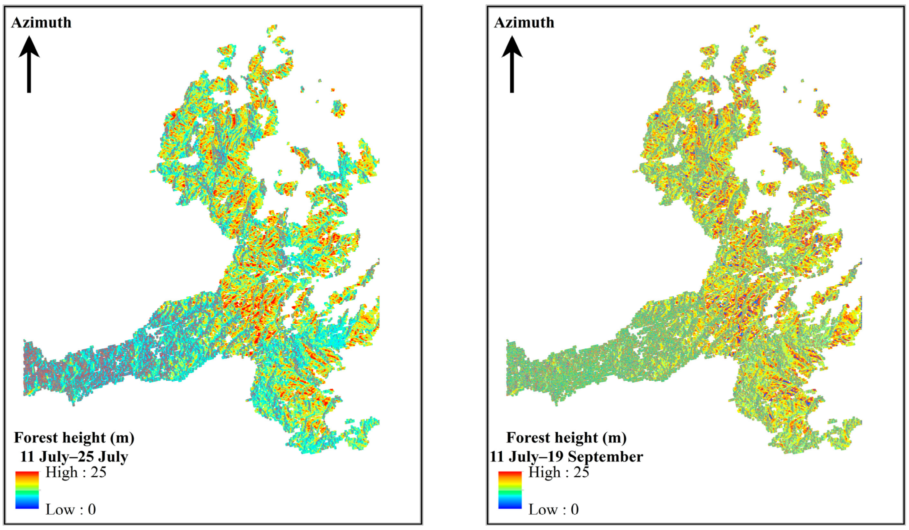

(**a**) (**b**)

Figure A4. Inversion results of forest height in the Saihanba under SAR coordinate system. (**a**) 11 July–25 July. (**b**) 11 July–19 September.

References

1. Chopping, M.; Nolin, A.; Moisen, G.G.; Martonchik, J.V.; Bull, M. Forest Canopy Height from the Multiangle Imaging SpectroRadiometer (MISR) Assessed with High Resolution Discrete Return Lidar. *Remote Sens. Environ.* **2009**, *113*, 2172–2185. [CrossRef]
2. Lu, D. The Potential and Challenge of Remote Sensing-Based Biomass Estimation. *Int. J. Remote Sens.* **2006**, *27*, 1297–1328. [CrossRef]
3. Radočaj, D.; Šiljeg, A.; Marinović, R.; Jurišić, M. State of Major Vegetation Indices in Precision Agriculture Studies Indexed in Web of Science: A Review. *Agriculture* **2023**, *13*, 707. [CrossRef]
4. Jung, H.; Won, J.; Kang, S.; Kim, S. Spatiotemporal Variability of Vegetation Response to Meteorological Drought on the Korean Peninsula. *Hydrol. Res.* **2023**, *54*, 1625–1640. [CrossRef]
5. Wang, Q.; Pang, Y.; Chen, D.; Liang, X.; Lu, J. Lidar Biomass Index: A Novel Solution for Tree-Level Biomass Estimation Using 3D Crown Information. *For. Ecol. Manag.* **2021**, *499*, 119542. [CrossRef]
6. Ali, N.; Khati, U. Forest Aboveground Biomass and Forest Height Estimation Over a Sub-Tropical Forest Using Machine Learning Algorithm and Synthetic Aperture Radar Data. *J. Indian Soc. Remote Sens.* **2024**. [CrossRef]
7. Mitchell, A.L.; Rosenqvist, A.; Mora, B. Current Remote Sensing Approaches to Monitoring Forest Degradation in Support of Countries Measurement, Reporting and Verification (MRV) Systems for REDD+. *Carbon Balance Manag.* **2017**, *12*, 9. [CrossRef]
8. Fomena, R.T.; Cloude, S.R. On the Role of Coherence Optimization in Polarimetric SAR Interferometry. *CEOS SAR Cal/Val Work.* **2005**, *22*, 9.
9. Lavalle, M.; Pottier, E.; Solimini, D.; Desnos, Y.L.; Miranda, N.; Rosich, B.; Santuari, M. A New Approach for Polinsar Forest Parameters Inversion: Results Using the ESA ALOS-PALSAR Prototype Processor. *Eur. Sp. Agency Spec. Publ. ESA SP* **2009**, *668*, 3–6.
10. Mette, T.; Kugler, F.; Papathanassiou, K.; Hajnsek, I. Forest and the Random Volume over Ground—Nature and Effect of 3 Possible Error Types. *Eur. Conf. Synth. Aperture Radar* **2006**, 1–4.
11. Cloude, S.R.; Papathanassiou, K.P. Three-Stage Inversion Process for Polarimetric SAR Interferometry. *IEE Proc. Radar Sonar Navig.* **2003**, *150*, 125–134. [CrossRef]
12. Tabb, M.; Carande, R. Robust Inversion of Vegetation Structure Parameters from Low-Frequency, Polarimetric Interferometric SAR. *Int. Geosci. Remote Sens. Symp.* **2001**, *7*, 3188–3190. [CrossRef]
13. Zebker, H.A.; Villasenor, J. Decorrelation in Interferometric Radar Echoes. *IEEE Trans. Geosci. Remote Sens.* **1992**, *30*, 950–959. [CrossRef]
14. Lei, Y.; Siqueira, P.; Clewley, D.; Lucas, R. Observation of Vegetation Vertical Structure and Disturbance Using L-Band InSAR over the Injune Region in Australia. In Proceedings of the International Geoscience and Remote Sensing Symposium (IGARSS), Munich, Germany, 22–27 July 2012; pp. 1637–1640. [CrossRef]
15. Lee, S.K.; Kugler, F.; Papathanassiou, K.P.; Hajnsek, I. Quantifying Temporal Decorrelation over Boreal Forest at L- And P-Band. In Proceedings of the 7th European Conference on Synthetic Aperture Radar, EUSAR, Friedrichshafen, Germany, 2–5 June 2008; pp. 1–4.
16. Lavalle, M.; Solimini, D.; Pottier, E.; Desnos, Y.L. The Dependence of the Polinsar Degree of Coherence on Forest Parameters. *Eur. Sp. Agency Spec. Publ.* **2009**, *SP-668*.

17. Zhang, Y.; Zhao, H.; Ji, Y.; Zhang, T.; Zhang, W. Forest Height Inversion via RVoG Model and Its Uncertainties Analysis via Bayesian Framework—Comparisons of Different Wavelengths and Baselines. *Forests* **2023**, *14*, 1408. [CrossRef]
18. Mao, Y.; Michel, O.O.; Yu, Y.; Fan, W.; Sui, A.; Liu, Z.; Wu, G. Retrieval of Boreal Forest Heights Using an Improved Random Volume over Ground (Rvog) Model Based on Repeat-Pass Spaceborne Polarimetric Sar Interferometry: The Case Study of Saihanba, China. *Remote Sens.* **2021**, *13*, 4306. [CrossRef]
19. Sa, R.; Nei, Y.; Fan, W. Combining Multi-Dimensional SAR Parameters to Improve RVoG Model for Coniferous Forest Height Inversion Using ALOS-2 Data. *Remote Sens.* **2023**, *15*, 1272. [CrossRef]
20. Bai, L.; Hong, W.; Cao, F. Estimation Error of Topographic Phase Based on RVoG Model Using POLinSAR Data. *Prog. Electromagn. Res. Symp.* **2009**, *2*, 1437–1441. [CrossRef]
21. Zhang, Q.; Mercer, B.; Cloude, S.R. Forest Height Estimation from INDREX-II L-Band Polarimetric InSAR Data. In Proceedings of the ISPRS XXIth Congress, Beijing, China, 3–11 July 2008; pp. 3–11.
22. Cloude, S.R.; Papathanassiou, K.P. Polarimetric SAR Interferometry. *IEEE Trans. Geosci. Remote Sens.* **1998**, *36*, 1551–1565. [CrossRef]
23. Managhebi, T.; Maghsoudi, Y.; Valadan Zoej, M.J. An Improved Three-Stage Inversion Algorithm in Forest Height Estimation Using Single-Baseline Polarimetric SAR Interferometry Data. *IEEE Geosci. Remote Sens. Lett.* **2018**, *15*, 887–891. [CrossRef]
24. Lavalle, M.; Simard, M.; Pottier, E.; Solimini, D. PolInSAR Forestry Applications Improved by Modeling Height-Dependent Temporal Decorrelation. In Proceedings of the 2010 IEEE International Geoscience and Remote Sensing Symposium, Honolulu, HI, USA, 25–30 July 2010; IEEE: Piscataway, NJ, USA, 2010; pp. 4772–4775. [CrossRef]
25. Pottier, E.; Ferro-Famil, L.; Allain, S.; Cloude, S.R.; Hajnsek, I.; Papathanassiou, K.; Moreira, A.; Williams, M.; Minchella, A.; Lavalle, M. Overview of the PolSARpro v4. 0 Software New Updates of the Educational Toolbox for Polarimetric and Interferometric Polarimetric SAR Data Processing. In Proceedings of the POLinSAR 2009, Frascati, Roma, 26–30 January 2009; p. CD-ROM.
26. Newell, R.G. Climate Change and Forest Sinks: Factors Affecting the and The Kyoto Protocol to the United Nations Framework Convention on Climate Change w 37 x Establishes the Principle That Carbon Sequestration Can Be Used By. *Enviornmental Econ. Manag.* **2000**, *40*, 211–235. [CrossRef]
27. Rosenqvist, A.; Shimada, M.; Suzuki, S.; Ohgushi, F.; Tadono, T.; Watanabe, M.; Tsuzuku, K.; Watanabe, T.; Kamijo, S.; Aoki, E. Operational Performance of the ALOS Global Systematic Acquisition Strategy and Observation Plans for ALOS-2 PALSAR-2. *Remote Sens. Environ.* **2014**, *155*, 3–12. [CrossRef]
28. Neumann, M. Remote Sensing of Vegetation Using Multi-Baseline Polarimetric SAR Interferometry: Theoretical Modeling and Physical Parameter Retrieval. Ph.D. Thesis, University Rennes, Rennes, France, 2009.
29. Chowdhury, T.A.; Thiel, C.; Schmullius, C. Growing Stock Volume Estimation from L-Band ALOS PALSAR Polarimetric Coherence in Siberian Forest. *Remote Sens. Environ.* **2014**, *155*, 129–144. [CrossRef]
30. Diakoulaki, D.; Mavrotas, G.; Papayannakis, L. Determining Objective Weights in Multiple Criteria Problems: The Critic Method. *Comput. Oper. Res.* **1995**, *22*, 763–770. [CrossRef]
31. Cloude, S.R. Polarization Coherence Tomography. *Radio Sci.* **2006**, *41*, 1–27. [CrossRef]
32. Lulu, T.; Ruliang, Y. Investigation on Tree Height Retrieval with Polarimetric Sar Interferometry. *Int. Geosci. Remote Sens. Symp.* **2008**, *5*, 546–549. [CrossRef]
33. Krieger, G.; Papathanassiou, K.P.; Cloude, S.R. Spaceborne Polarimetric SAR Interferometry: Performance Analysis and Mission Concepts. *EURASIP J. Appl. Signal Process.* **2005**, *2005*, 3272–3292. [CrossRef]
34. Askne, J.I.H.; Dammert, P.B.G.; Ulander, L.M.H.; Smith, G. C-Band Repeat-Pass Interferometric SAR Observations of the Forest. *Doktorsavhandlingar Vid Chalmers Tek. Hogsk.* **1999**, *35*, 25–35. [CrossRef]
35. Cloude, S. *Polarisation: Applications in Remote Sensing*; OUP: Oxford, UK, 2009.
36. Lei, Y.; Siqueira, P.; Torbick, N.; Ducey, M.; Chowdhury, D.; Salas, W. Generation of Large-Scale Moderate-Resolution Forest Height Mosaic with Spaceborne Repeat-Pass SAR Interferometry and Lidar. *IEEE Trans. Geosci. Remote Sens.* **2019**, *57*, 770–787. [CrossRef]
37. Liao, Z.; He, B.; Quan, X.; van Dijk, A.I.J.M.; Qiu, S.; Yin, C. Biomass Estimation in Dense Tropical Forest Using Multiple Information from Single-Baseline P-Band PolInSAR Data. *Remote Sens. Environ.* **2019**, *221*, 489–507. [CrossRef]